electrons and formation of nonregular TCNQ chains, probably tetramerized. Such tetramerization can be the result of a specific interaction between TCNQ and dipole moments of cations. In this situation a systematic temperature change in the activation energy, E_a, can occur.

Conclusions

TCNQ complex salts with metallocene ions represent an interesting class of semiconducting organometallic compounds. Their transport and spectral properties are determined by the appearance of TCNQ chains. At high temperature the chains are nearly uniform, with delocalized electrons. This delocalization is seen from both spectral and transport properties. At low temperature the salts are characterized by nonregular charge distribution along the chains. This is shown not only by the appearance of the energy gap at about 0.3 eV (and as a consequence the thermally activated electrical conductivity and strongly T dependent thermoelectric power) but also directly by the presence of the new absorption bands characteristic of $TCNQ^{\delta-}$ with $0.3 < \delta < 0.6$.

The physical properties of TCNQ salts with metallocene ions are not unusual for organic low-dimensional conductors. The large, three-dimensional ions do not cause significant changes in the properties of the salts. This points to a secondary role for the counterions in TCNQ salts. However, in order to achieve a definitive interpretation of the properties of the salts, it appears necessary to include studies of other phenomena, especially spin ordering, for which ESR measurements will soon be carried out.

Contribution from the Research School of Chemistry, Australian National University, Canberra, ACT 2601, Australia, Institut für anorganische Chemie, Universität Basel, Basel, Switzerland, and Department of Chemistry, University of Canterbury, Christchurch, New Zealand

Electronic and Molecular Structure of $[Cr(bpy)_3]^{3+}$ (bpy = 2,2′-Bipyridine)

A. Hauser,*† M. Mäder,‡ W. T. Robinson,§ R. Murugesan,† and J. Ferguson†

Received October 7, 1986

$[Cr(bpy)_3](PF_6)_3$ and $[Rh(bpy)_3](PF_6)_3$ both crystallize in the trigonal space group $R32$, with site symmetry D_3 for the metal ions. Absorption and Zeeman spectra of neat $[Cr(bpy)_3](PF_6)_3$ and dilute $[Rh(bpy)_3](PF_6)_3:Cr^{3+}$ in the region of ligand field transitions as well as emission spectra and EPR of the latter have been studied. Ground-state ($^4A_2$) and first-excited-state (^2E) zero-field splittings and g values for Cr^{3+} and assignments of bands at higher energy to $^4A_2 \rightarrow {}^2T_1$ electronic origins are reported. The fine structure in the region of the $^4A_2 \rightarrow {}^4T_2$ and $^2T_2$ transitions is ascribed to vibrational sidebands of the former.

1. Introduction

Cr^{3+} coordination compounds have received a lot of attention over the last two decades. The initial papers by Sugano et al.[1,2] on the electronic structure of the $^4A_2$ ground state and the ^2E, $^2T_1$, and $^2T_2$ excited states in a trigonally distorted ligand field (LF) gave the incentive for a lot of experimental and theoretical work[2-4] mainly on Cr^{3+} doped into crystal lattices containing oxygen as the coordinating ligand, such as ruby, emerald, spinels, and garnets. For these compounds it has generally been possible to account for the low-lying metal-centered energy levels, and their zero-field splittings and g values, by diagonalizing the full d^3 LF matrix, including an axial component along the trigonal axis and an external magnetic field together with the octahedral LF, the electrostatic interaction, and spin–orbit coupling.[5] The inclusion of the two trigonal LF parameters K and K' (as defined by Sugano and Tanabe[1]) in the calculation was particularly successful in rationalizing the zero-field splitting of the $^4A_2$ ground state, the zero-field splittings of the ^2E, $^2T_1$, and $^2T_2$ excited states, and the g values of the ^2E components. All of these quantities depend largely on K and K' and to some extent on the spin–orbit coupling constant ζ and are more or less independent of the Racah parameters B and C and the octahedral part of the LF $10Dq$, which basically determine the absolute energy of the various energy levels but not their splittings.

Cr^{3+} coordination compounds with nitrogen-containing ligands have been studied over the last few years in quite a different context. It was and still is their photoactivity that makes them attractive.[6] Most investigations of nitrogen-coordinated Cr^{3+} compounds have therefore centered around their photochemistry, observed mainly in solution and glasses,[7] and the elucidation of the electronic structure has been somewhat neglected. Solomon et al.[8] have performed an analysis of the $^4A_2 \rightarrow {}^4T_2$ d–d transition in $[Cr(NH_3)_6](ClO_4)_2Cl{\cdot}KCl$ on the basis of a dynamic Jahn–Teller effect, and Güdel et al.,[9] McCarthy and Vala,[10] and Geiser and Güdel[11] have done some optical measurements on $2[Cr(en)_3]Cl_3{\cdot}KCl{\cdot}6H_2O$.

However, in order to come to grips with the photochemical behavior of nitrogen-coordinated Cr^{3+} compounds, it seems to us to be of prime importance to know what the electronic structure of a given species is, paying special attention to its molecular symmetry. This prompted us to study $[Cr(bpy)_3]^{3+}$ (bpy = 2,2′-bipyridine) both as the pure PF_6^- salt and in a dilute form, doped into isostructural $[Rh(bpy)_3](PF_6)_3$. The advantage of these compounds is that the inherent molecular symmetry of the $[Cr(bpy)_3]^{3+}$, namely D_3, is retained in the crystal lattice.

In this paper the single-crystal X-ray structures of both $[Cr(bpy)_3](PF_6)_3$ and $[Rh(bpy)_3](PF_6)_3$, single-crystal and powder EPR spectra of $[Rh(bpy)_3](PF_6)_3:Cr^{3+}$, and the low-temperature absorption spectra of both the neat and the dilute material in the region of d–d transitions as well as the low-temperature emission spectrum of the dilute material are reported. A full d^3 LF calculation, including the electrostatic interaction, the octahedral and trigonal parts of the LF, spin–orbit coupling, and an external magnetic field, was carried out in order to interpret the experimental results quantitatively.

2. Experimental Section

Synthesis and Crystal Growth. $[Rh(bpy)_3](PF_6)_3$.[12] A 0.5-g sample

(1) Sugano, S.; Tanabe, Y. *J. Phys. Soc. Jpn.* **1958**, *13*, 880.
(2) Sugano, S.; Tsujikawa, J. *J. Phys. Soc. Jpn.* **1958**, *13*, 899.
(3) McFarlane, R. M. *J. Chem. Phys.* **1962**, *39*, 3118.
(4) McFarlane, R. M. *Phys. Rev. B: Solid State* **1970**, *1*, 989.
(5) McFarlane, R. M. *J. Chem. Phys.* **1967**, *47*, 2066.
(6) Endicott, J. F. *J. Chem. Educ.* **1983**, *60*, 824.
(7) Allsop, S. R.; Cox, A.; Kemp, T. J.; Reed, W. J. *J. Chem. Soc., Faraday Trans. 1* **1980**, *76*, 162.
(8) Wilson, R. B.; Solomon, E. I. *Inorg. Chem.* **1978**, *17*, 1729.
(9) Güdel, G. U.; Trabjerg, I. B.; Vala, M.; Ballhausen, C. J. *Mol. Phys.* **1972**, *24*, 1227.
(10) McCarthy, P. J.; Vala, M. *Mol. Phys.* **1973**, *25*, 17.
(11) Geiser, U.; Güdel, H. U. *Inorg. Chem.* **1981**, *20*, 3013.
(12) Harris, C. M.; McKenzie, E. D. *J. Inorg. Nucl. Chem.* **1963**, *25*, 171.

† Australian National University.
‡ Universität Basel.
§ University of Canterbury.

0020-1669/87/1326-1331$01.50/0

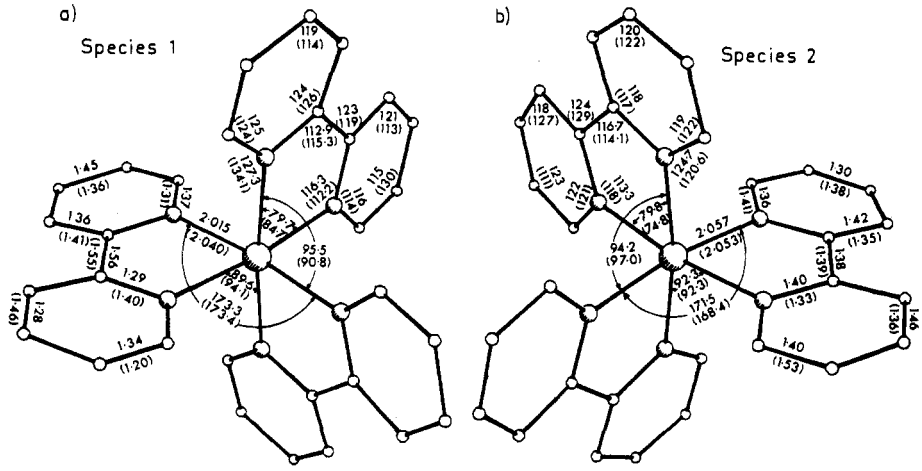

Figure 1. Bond lengths (Å) and bond angles (deg) of the two species of $M(bpy)_3^{3+}$ (M = Rh, Cr) complexes present in the crystal structure. The numbers in parentheses refer to $[Cr(bpy)_3](PF_6)_3$, those without to $[Rh(bpy)_3](PF_6)_3$.

of $RhCl_3 \cdot 3H_2O$ and 1.2 g of bpy were refluxed for 20 h in 50% ethanol/water. After the solution was boiled with animal charcoal and filtered, the PF_6^- salt was precipitated by addition of a saturated aqueous solution of $NaPF_6$. Single crystals suitable for an X-ray structure determination were grown in the dark by slow evaporation of the saturated, slightly acidified aqueous solution.

$[Cr(bpy)_3](PF_6)_3$.[13] A 10-g sample of bpy was dissolved in 300 mL of H_2O by addition of $HClO_4$ (~7 mL) to give a pH of 2. After degassing, 2.5 g of $CrCl_2$ (Pfaltz & Bauer, Stamford, CT) was added under vigorous stirring to give a dark purple suspension of $[Cr(bpy)_3](ClO_4)_2$. The chromous complex was oxidized by bubbling oxygen through the suspension until a clear yellow solution was obtained. The perchlorate salt was transformed into the highly soluble nitrate on an anion-exchange column, and addition of saturated $NaPF_6$ precipitated the hexafluorophosphate. Single crystals were grown in the dark by slow evaporation of the slightly acidified aqueous solutions. Mixed crystals were grown in the same manner from mixed solutions.

X-ray Single-Crystal Data Collection and Treatment. Crystal data, established from precession photographs, were accurately measured on a Nicolet XRD P3 four-circle diffractometer, using Mo K$\bar{\alpha}$ radiation from a crystal monochromator (λ(Mo K$\bar{\alpha}$) = 0.71069 Å). The $\theta/2\theta$ scan technique was used to collect reflection intensities out to maximum Bragg angles of 22.5° for $[Rh(bpy)_3](PF_6)_3$ and 25° for $[Cr(bpy)_3](PF_6)_3$. The number of independent reflections measured was 1234 (971 with $I > 2\sigma$) for the rhodium and 1229 (592 with $I > 3\sigma$) for the chromium compound. Absorption corrections were not applied. Accurate unit cell parameters were determined from 25 accurately centered reflections (25° < 2θ < 35°). The important crystal information for the two structures is listed in Table I.

Structure Solution and Refinements. The rhodium structure was solved by heavy-atom vector methods and difference Fourier syntheses. The starting model for the chromium structure contained the refined rhodium structure coordinates. Blocked-cascade least-squares refinements (SHELXTL[14]) were employed, with the weights $1/(\sigma^2(|F|) + g(|F|^2))$ being applied to reflection data. The function minimized was $\sum w(|F_o| - |F_c|)^2$. Anomalous dispersion coefficients were taken from Cromer and Liberman.[15] Although hydrogen atom positions were clearly revealed from difference synthesis for the rhodium compound, they were refined in the models from idealized coordinates geometrically calculated with C–H bonds of 0.96 Å. Final Fourier synthesis showed no significant residual electron density, and there were no significant discrepancies between observed and calculated structure factors. The results of the structure refinements are listed in Table I.

EPR. EPR spectra were recorded at Q-band frequency on a Varian V-4503 spectrometer using a 35-GHz Model V-4561 microwave bridge and a TE_{011} mode cylindrical cavity. For both single-crystal and powder measurements samples of $[Rh(bpy)_3](PF_6)_3$ doped with 5% Cr^{3+} were used. A single crystal ~0.4 × ~0.4 × ~3 mm³ was mounted on the face of a precision-cut quartz rod (3-mm diameter), the other end of which was fitted with a goniometer. The resulting accuracy of crystal alignment with respect to the magnetic field was ±1°. The magnetic field

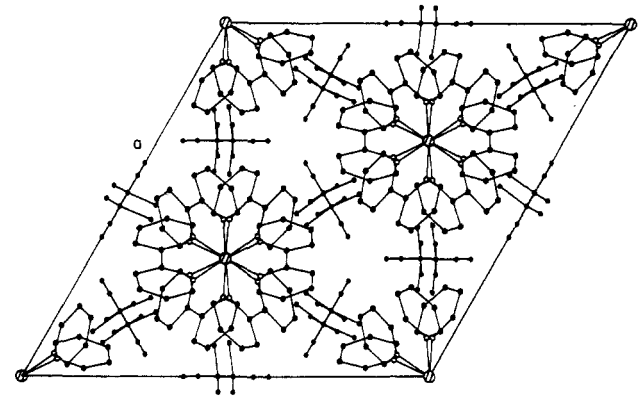

Figure 2. Projection of the unit cell down the unique axis.

was calibrated by using a Gaussmeter, and the microwave frequency was taken from the meter on the bridge. In addition, DPPH was used as an internal field marker. Temperatures down to 85 K were achieved with a cold nitrogen gas flow technique.

Visible Optical Spectroscopy. Polarized single-crystal optical absorption spectra were generated from single-beam transmission spectra recorded with a computer-controlled $^3/_4$-m Czerny-Turner monochromator (Spex 1702) with a grating blazed at 500 nm for light dispersion, a 150-W tungsten lamp as light source, and a Glan-Taylor polarizer to polarize and an EMI 9558 photomultiplier tube to detect the light. An 800-Hz tuning-fork chopper together with a lock-in amplifier (PAR 117) served to reduce the effect of dark current.

Sample temperatures down to 1.4 K and magnetic fields up to 5 T were achieved with an Oxford Instruments SM5 Cryostat equipped with a variable-temperature insert. Crystals were mounted on copper disks with matched holes, which in turn were mounted on the sample holder so that the magnetic field was either parallel or perpendicular to the crystal c axis, easily identified as such between crossed polarizers. The crystal dimensions were 0.175 × ~0.2 × ~2.5 mm³ for the neat $[Cr(bpy)_3](PF_6)_3$ and ~0.4 × ~0.4 × ~3 mm³ for the dilute $[Rh(bpy)_3](PF_6)_3$:Cr(~5%).

3. Results and Discussion

3.1. Crystal Structures. $[Rh(bpy)_3](PF_6)_3$ and $[Cr(bpy)_3](PF_6)_3$ are isostructural; they belong to the trigonal space group $R32$. There are six $[M(bpy)_3]^{3+}$ (M = Rh, Cr) cations in the unit cell. The metal atoms are located on the independent special positions (0, 0, 0) and (0, 0, $^1/_2$) with site geometry D_3-32. The three bpy ligands around one metal atom form a propeller-like trigonal arrangement. The coordination of the metal atoms is close to octahedral, deviations consisting of a compression of the coordination octahedron along the trigonal axis and a twisting of the three nitrogen atoms in one plane perpendicular to the trigonal axis with respect to the three in the other plane. In Figure 1 bond lengths and bond angles for the two independent cations of both the rhodium and the chromium structure are shown. The

(13) Baker, R. B.; Mehta, B. D. *Inorg. Chem.* **1965**, *4*, 848.
(14) Sheldick, G. M. *SHELXTL User Manual*; Nicolet XRD Corp.: Cupertino, CA, 1983.
(15) Cromer, D. T.; Liberman, D. *J. Chem. Phys.* **1970**, *53*, 1891.

Table I. Crystallographic Data

	$[Rh(bpy)_3](PF_6)_3$	$[Cr(bpy)_3](PF_6)_3$
mol wt	1006.4	945.5
cryst dimens, mm^3	0.4 × 0.4 × 0.3	0.5 × 0.4 × 0.3
space group	*R*32	*R*32
Z	6	6
cell params		
a, Å	18.072 (2)	18.016 (3)
c, Å	19.919 (3)	20.017 (4)
V, $Å^3$	5634 (2)	5635 (2)
d_{calcd}, g/cm^3	1.78	1.67
d_{expt}, g/cm^3	1.76	1.68
μ(Mo Kα), cm^{-1}	6.8	5.4
g	0.0004	0.0013
no. of indep reflcns	1234	1229
max θ, deg	22.5	25.0
R^a	0.036	0.048
R_w^b	0.049	0.059
axial distortion: angle between *c* axis and M–N bond (54.74° in octahedron)		
species 1	58.7	55.3
species 2	57.8	59.9
twist angle: vertical projection of N–M–N angle (30° in octahedron)		
species 1	26.1	26.0
species 2	25.0	23.3

$^a R = \sum||F_o| - |F_c||$. $^b R_w = [\sum w(|F_o| - |F_c|)^2/\sum w|F_o|^2]^{1/2}$; $w = (1/\sigma)(|F_o|^2)$.

molecular trigonal axis of both species is parallel to the 3-fold crystal axis. As cations centered on (0, 0, 0) have opposite chirality to those on (0, 0, $^1/_2$), cations of opposite chirality alternate along the 3-fold axis of the hexagonal unit cell. These enantiomeric cations are approximately staggered with respect to each other, as illustrated in Figure 2. However, the perfect centrosymmetric distribution of the rhodium and chromium atoms, respectively, makes it difficult to establish the space group polarity, i.e. the absolute configuration of, e.g., the $[Ru(bpy)_3]^{3+}$ unit in the (0, 0, 0) position of a given crystal. For the rhodium compound the inverted structure gave $R = 0.037$ and $R_w = 0.050$, as compared to $R = 0.036$ and $R_w = 0.049$ for the orientation shown in Figures 1 and 2. No similar, significant, difference resulted from the poorer data on the chromium compound.

All phosphorus atoms and the fluorine atoms F(13), F(14), F(23), and F(24) are located on 2-fold axes, corresponding to the special positions of types (*x*, 0, 0) and (*x*, 0, $^1/_2$). The remaining fluorine atoms are in general positions. The P–F distances in the rhodium compound range from 1.54 (1) to 1.63 (1) Å. In Table II positional and thermal parameters as well as their estimated standard deviations are given.

3.2. EPR of $[Rh(bpy)_3](PF_6)_3$:Cr^{3+}. EPR is one of the most widely used techniques in the study of ground-state properties of paramagnetic transition-metal ions such as the $^4A_2$ ground state of Cr^{3+}.[16] Figure 3a shows the $\nu = 35$ GHz EPR powder spectrum of $[Rh(bpy)_3](PF_6)_3$:Cr^{3+} at 293 K. From the large spread of the observed lines and the high intensity of the "forbidden" line at low field, it is evident that the zero-field splitting (zfs) due to higher order spin–orbit coupling and a low-symmetry LF is large, so large in fact that some of the high-field transitions are outside the range of our magnet ($H_{max} = 17.5$ kG). This together with the comparatively large line widths of the lines limits the accuracy of *g* values and zfs obtained from this spectrum. A single-crystal EPR study was therefore indicated. Figure 3b shows the single-crystal EPR spectra of $[Rh(bpy)_3](PF_6)_3$:Cr^{3+} at selected angles between $H \parallel c$ ($\theta = 0°$) and $H \perp c$ ($\theta = 90°$) and the detailed angular dependence of the observed lines. The $H \perp c$ spectrum was found to be invariant under rotation around *c*,

(16) Goodman, B. A.; Raynor, J. B. In *Advances in Inorganic Chemistry*; Emeleus, H. J., Sharpe, A. G., Eds.; Academic: New York, 1970; Vol. 13.

Table II. Positional and Thermal Parameters and Their Estimated Standard Deviations

atom	*x*	*y*	*z*	B_{eqv}, $Å^2$
	(a) $[Rh(bpy)_3](PF_6)_3$			
Rh(1)	1.0000	1.0000	1.0000	0.27 (1)
N(1)	0.9516 (3)	0.8902 (4)	0.9475 (3)	0.41 (2)
C(12)	0.9763 (7)	0.8374 (7)	0.9656 (5)	0.33 (4)
C(13)	0.9597 (5)	0.7660 (4)	0.9309 (4)	0.45 (3)
C(14)	0.9178 (8)	0.7473 (6)	0.8758 (7)	0.55 (5)
C(15)	0.8873 (10)	0.8025 (8)	0.8509 (4)	0.50 (7)
C(16)	0.9067 (5)	0.8708 (6)	0.8888 (3)	0.50 (4)
Rh(2)	1.0000	1.0000	0.5000	0.29 (1)
N(2)	0.8892 (3)	0.9361 (3)	0.5550 (2)	0.30 (2)
C(22)	0.8309 (3)	0.8559 (7)	0.5284 (5)	0.37 (4)
C(23)	0.7582 (5)	0.8013 (5)	0.5673 (4)	0.55 (4)
C(24)	0.7457 (8)	0.8341 (10)	0.6308 (5)	0.59 (7)
C(25)	0.7998 (8)	0.9121 (11)	0.6494 (7)	0.64 (7)
C(26)	0.8728 (4)	0.9661 (5)	0.6125 (4)	0.47 (3)
P(1)	0.5200 (3)	1.0000	1.0000	0.54 (2)
F(11)	0.5418 (6)	1.0445 (5)	0.9287 (3)	1.25 (5)
F(12)	0.4838 (7)	0.9123 (11)	0.9661 (3)	1.44 (6)
F(13)	0.6035 (5)	1.0000	0.0000	1.38 (10)
F(14)	0.4313 (7)	1.0000	0.0000	1.64 (9)
P(2)	0.4817 (4)	1.0000	0.5000	0.58 (2)
F(21)	0.5392 (5)	1.0943 (4)	0.5284 (3)	1.06 (3)
F(22)	0.4610 (5)	0.9563 (4)	0.5719 (3)	0.93 (12)
F(23)	0.3952 (6)	1.0000	0.5000	1.87 (12)
F(24)	0.5668 (6)	1.0000	0.5000	1.89 (12)
H(13)	0.9809	0.7300	0.9469	0.91
H(14)	0.9053	1.0234	0.8517	0.64
H(15)	0.8562	0.7914	0.8095	0.48
H(16)	0.8873	0.9087	0.8738	0.87
H(23)	0.7178	0.7451	0.5515	0.44
H(24)	0.6984	0.7974	0.6591	0.66
H(25)	0.7882	0.9334	0.6898	0.82
H(26)	0.9111	1.0234	0.6274	0.38
	(b) $[Cr(bpy)_3](PF_6)_3$			
Cr(1)	1.0000	1.0000	1.0000	0.37 (2)
N(1)	0.9529 (5)	0.8927 (5)	0.9420 (4)	0.44 (4)
C(12)	0.9754 (5)	0.8339 (7)	0.9663 (5)	0.38 (4)
C(13)	0.9627 (12)	0.7596 (13)	0.9330 (7)	0.43 (9)
C(14)	0.9204 (11)	0.7477 (12)	0.8686 (10)	0.54 (9)
C(15)	0.8946 (9)	0.8057 (7)	0.8559 (5)	0.59 (7)
C(16)	0.9076 (6)	0.8679 (6)	0.8871 (5)	0.38 (5)
Cr(2)	1.0000	1.0000	0.5000	0.32 (2)
N(2)	0.8870 (5)	0.9319 (5)	0.5515 (4)	0.30 (3)
C(22)	0.8322 (10)	0.8530 (10)	0.5307 (9)	0.41 (7)
C(23)	0.7627 (14)	0.8061 (13)	0.5692 (13)	0.73 (11)
C(24)	0.7435 (16)	0.8300 (16)	0.6281 (12)	0.78 (14)
C(25)	0.7965 (7)	0.9089 (8)	0.6564 (5)	0.51 (6)
C(26)	0.8739 (8)	0.9635 (9)	0.6121 (6)	0.66 (7)
P(1)	0.5213 (3)	1.0000	1.0000	0.50 (3)
F(11)	0.5439 (13)	1.0427 (9)	0.9297 (7)	1.32 (12)
F(12)	0.4938 (11)	0.9142 (7)	0.9647 (5)	1.83 (13)
F(13)	0.6083 (6)	1.0000	0.0000	1.11 (10)
F(14)	0.4309 (8)	1.0000	0.0000	1.50 (10)
P(2)	0.4762 (3)	1.0000	0.5000	0.74 (3)
F(21)	0.5394 (6)	1.0920 (5)	0.5261 (4)	1.03 (5)
F(22)	0.4564 (9)	0.9532 (8)	0.5717 (9)	1.03 (10)
F(23)	0.3994 (11)	1.0000	0.5000	3.15 (34)
F(24)	0.5549 (9)	1.0000	0.5000	3.25 (29)
H(13)	0.9820	0.7226	0.9505	0.91
H(14)	0.9114	0.7021	0.8388	0.64
H(15)	0.8592	0.7935	0.8170	0.48
H(16)	0.8859	0.9033	0.8704	0.87
H(23)	0.7214	0.7500	0.5533	0.44
H(24)	0.6923	0.7912	0.6519	0.66
H(25)	0.7876	0.9278	0.6989	0.82
H(26)	0.9129	1.0216	0.6250	0.38

a result expected from the crystal structure since the molecular trigonal axis of the $[M(bpy)_3]^{3+}$ (M = Rh, Cr) complexes is parallel to the crystallographic *c* axis. This means that it should be possible to analyze the EPR spectra in terms of the axially symmetric spin Hamiltonian[17]

$$\hat{H} = g_\parallel \mu_B H_z S_z + g_\perp \mu_B [H_x S_x + H_y S_y] + D[S_z^2 - {}^1/_3 S(S+1)] \quad (1)$$

Table III. Experimental Zero-Field Splittings and g Values for the $^4A_2$ Ground State and the ^2E Excited State

	temp, K	$[Cr(bpy)_3](PF_6)_3$	$[Rh(bpy)_3](PF_6)_3:Cr^{3+}$	$2[Cr(en)_3]Cl_3 \cdot KCl \cdot H_2O$
		$^4A_2$		
		EPR		
$g_\parallel$	293		1.984	1.986[a]
$g_\perp$			1.976	1.982
$\lvert 2D\rvert$, cm^{-1}			0.998	0.0427
$\lvert 2D\rvert$, cm^{-1}	85		1.038	
		Optical		
$2D$, cm^{-1}	4.2	−0.82 (2)	−1.03 (4)	
		^2E		
		Optical		
$D(^2E)$, cm^{-1}	1.4	−19.5	−19.6	19.0[b]
$g_\parallel(2\bar{A})$		2.68[c]	2.23[c]	2.61
$g_\parallel(\bar{E})$		−1.82	−1.71	−1.47
$g_\parallel(2\bar{A})$	12	2.38[d]		
$g_\parallel(\bar{E})$		−1.55		
		$^2T_1$		
		Optical		
$g_\parallel(2\bar{A})$		3.5[c]		

[a] Measured in $2[Rh(en)_3]Cl_3 \cdot KCl \cdot 6H_2O$ containing ~2% Cr^{3+}.[20] [b] References 9 and 11. [c] From shifts in 1.4 K absorption and emission spectra. [d] From splittings in 12 K spectra.

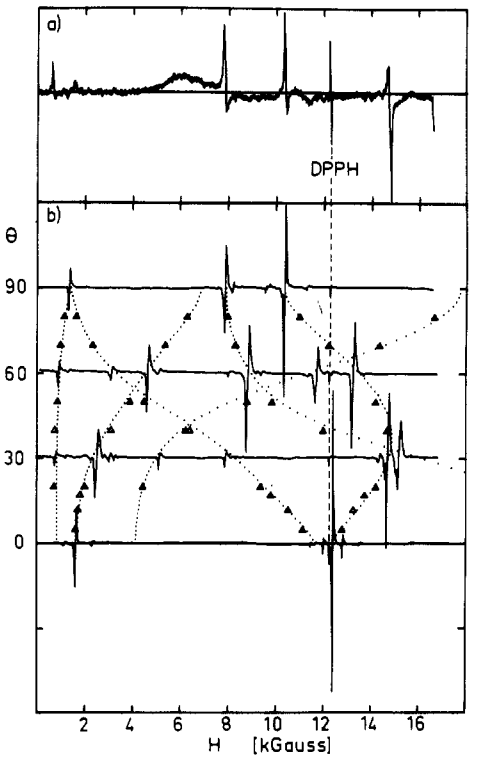

Figure 3. (a) EPR powder spectrum of $[Rh(bpy)_3](PF_6)_3:Cr^{3+}$(~5%). (b) Single-crystal EPR spectra at selected angles θ ($\theta = 0°$, $H \parallel c$; $\theta = 90°$, $H \perp c$): (Δ) experimental line positions at some intermediate angles; (···) line positions calculated by using parameters from Table III.

which gives a zfs of $2D = E(\pm^3/_2) - E(\pm^1/_2)$ between the components of the ground state. At $\theta = 0°$ ($H_x = H_y = 0$) three allowed transitions with $\Delta m_s = \pm 1$ are expected, namely the $-^1/_2 \rightarrow {}^1/_2$ transition at $H_0 = \nu/(g_\parallel \mu_B)$ flanked by the $-^3/_2 \rightarrow -^1/_2$ and the $^1/_2 \rightarrow {}^3/_2$ transitions at $\Delta H = \pm 2D/(g_\parallel \mu_B)$. In the experimental $\theta = 0°$ spectrum the high-field line is out of the range of our magnet. The remaining two lines are sufficient to extract $g_\parallel$ = 1.984 and the magnitude of $|2D| = 0.998$ cm^{-1} but prevent us from fixing its sign, which in principle could be determined from the relative intensities of the low-field and the missing high-field line at low temperature. Due to the large zfs it is no longer possible to talk about "forbidden" and "allowed" transitions for $\theta \neq 0°$, and lines that in the limit of small zfs correspond to $\Delta m_s = \pm 2$, and are therefore weak, become quite strong. Therefore, the angular dependence of the resonance lines has to be analyzed by a full diagonalization of the Hamiltonian (1), calculating both line positions and relative intensities. The results of such a calculation are included in Figure 3b. $g_\perp = 1.976$ was determined from the best fit to the $H \perp c$ spectrum.

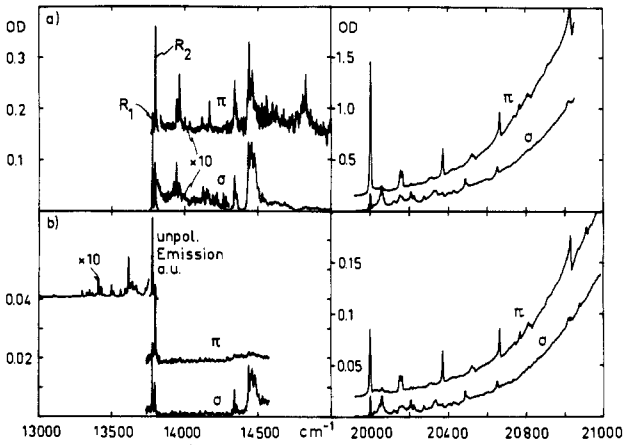

Figure 4. Polarized absorption spectra at 1.4 K in the regions of the $^4A_2 \rightarrow {}^2E$, $^2T_1$ (left-hand panels) and the $^4A_2 \rightarrow {}^4T_2$, $^2T_2$ (right-hand panels) transitions of (a) $[Cr(bpy)_3](PF_6)_3$ and (b) $[Rh(bpy)_3](PF_6)_3:Cr^{3+}$(~5%) and the unpolarized emission spectrum of the latter at 10 K. For the neat compound the crystal thickness $d = 0.175$ mm and [Cr] = 1.72 mol/L.

Comparison of the powder spectra at 293 and 85 K showed that $|2D|$ increases by ~4% as the temperature is lowered, due to the thermal contraction of the unit cell.

The hyperfine structure due to ^{53}Cr ($I = {}^3/_2$, natural abundance 9.54%), which usually shows up as a quartet of weak shoulders on the central line from the nonmagnetic chromium nuclei, cannot be observed in our case because of the comparatively large line width (~60 G) of the central line, even in the single crystal. This rather large line width could either be due to inhomogeneous line broadening, as a concentration of 5% Cr^{3+} is already quite large, or due to the fact that the unit cell actually contains two distinct although very similar species with just slightly different parameters.

The anisotropy of the g values is small and well within the range observed for Cr^{3+} coordination compounds.[17] From the reduction of the spin-only value $g_e = 2.0023$, the spin–orbit coupling constant ζ can be estimated according to the formula[18]

$$g = g_e - 8\zeta/3\Delta \qquad (2)$$

where $\Delta = 10Dq$, the separation between the $^4A_2$ ground state and the $^4T_2$ excited state. With $\Delta = 23\,400$ cm^{-1} [19] and g_{av}, we estimate $\zeta \approx 200$ cm^{-1}, as compared to the free-ion value of $\zeta_{free} = 273$ cm^{-1}.[18]

3.3. Optical Properties of $[Cr(bpy)_3](PF_6)_3$ and $[Rh(bpy)_3](PF_6)_3:Cr^{3+}$. Optical spectroscopy is the only direct way of gaining insight into the electronic structure of the excited states of a system. Figure 4 shows the polarized overall spectra in the region of d–d transitions, i.e. the spin-forbidden $^4A_2 \rightarrow {}^2E$, $^2T_1$, and $^2T_2$ and the spin-allowed $^4A_2 \rightarrow {}^4T_2$ transitions (O_h symmetry), for both neat $[Cr(bpy)_3](PF_6)_3$ and dilute $[Rh(bpy)_3](PF_6)_3:Cr^{3+}$. In Figure 4b the unpolarized emission spectrum of the dilute material is included. Rough assignments of the various band systems can be made on the basis of an octahedral LF calculation with the

(17) McGarvey, B. R. *J. Chem. Phys.* **1964**, *41*, 3743.
(18) Griffith, J. S. *The Theory of Transition Metal Ions*; Cambridge University Press: Cambridge, U.K., 1961.
(19) Kõnig, E.; Herzog, S. *J. Inorg. Nucl. Chem.* **1970**, *32*, 585.

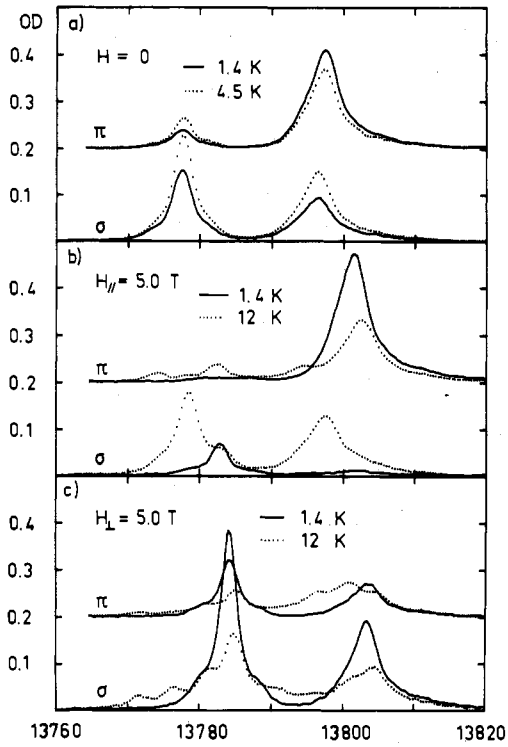

Figure 5. Polarized absorption and Zeeman spectra of the $^4A_2 \rightarrow {}^2E$ electronic origins in $[Cr(bpy)_3](PF_6)_3$: (a) $H = 0$; (b) $H \parallel c = 5.0$ T; (c) $H \perp c = 5.0$ T.

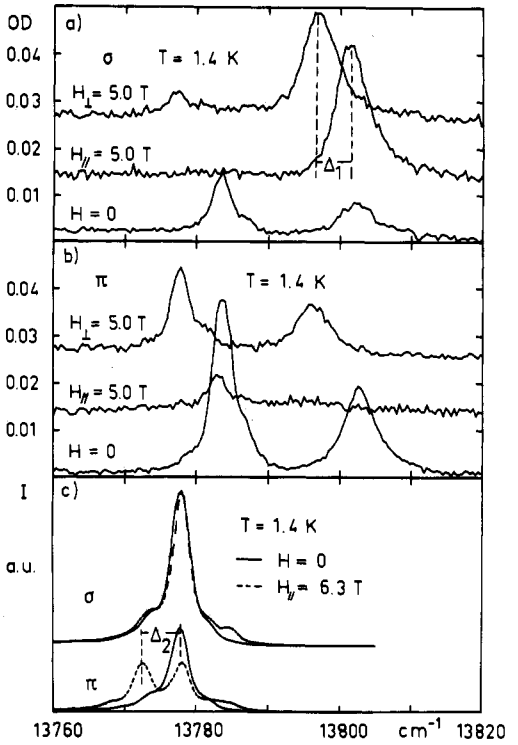

Figure 6. (a, b) Polarized absorption and Zeeman spectra of the $^4A_2 \rightarrow {}^2E$ electronic origins in $[Rh(bpy)_3](PF_6)_3:Cr^{3+}(\sim 5\%)$ at 1.4 K. (c) Polarized emission spectra of the $^4A_2 \leftarrow {}^2E$ electronic origins with and without an external magnetic field.

Racah parameters $B = 730$ cm^{-1} and $C = 2730$ cm^{-1} (both reduced by the same factor $\beta = 0.71$ from the free-ion value[20]) and $10Dq = 23\,400$ cm^{-1} from the $^4A_2 \rightarrow {}^4T_2$ band maximum.[19] The two sharp lines near 13 800 cm^{-1} are assigned to the $^4A_2 \rightarrow {}^2E$ electronic origins and the group of lines near 14 450 cm^{-1} to $^4A_2 \rightarrow {}^2T_1$. Vibronic sidebands of these two transitions are much weaker than the electronic origins. The assignment of the absorption lines between 20 000 and 22 000 cm^{-1} is not as straightforward. The $^4A_2 \rightarrow {}^2T_2$ and the $^4A_2 \rightarrow {}^4T_2$ electronic origins are expected to be close together, and the presence of low-lying charge-transfer states further complicates matters.

3.3.1. The $^4A_2 \rightarrow {}^2E$ Transition. Figure 5a shows the polarized absorption spectra of neat $[Cr(bpy)_3](PF_6)_3$ in the region of the two electronic origins (R_1 and R_2) of the $^4A_2 \rightarrow {}^2E$ transition at 1.4 and 4.5 K. Parts b and c of Figure 5 show the effects on R_1 and R_2 of an external magnetic field H of 5 T parallel and perpendicular to the c axis. Parts a and b of Figure 6 show the same thing for dilute $[Rh(bpy)_3](PF_6)_3:Cr^{3+}$. In both cases, the lines are split by 19.5 (5) cm^{-1} due to the axial component in the ligand field and spin–orbit coupling and their intensities show a marked temperature dependence even with $H = 0$ T. The total oscillator strength in σ polarization (E perpendicular to c) is $f_\sigma \sim 2.6 \times 10^{-7}$ and in π polarization (E parallel to c) $f_\pi \sim 1.6 \times 10^{-7}$. The maximum magnetic dipole (md) oscillator strength to be expected for these transitions is $\sim 5 \times 10^{-9}$,[18] almost 2 orders of magnitude less. Therefore the observed intensity is of electric dipole (ed) origin, and since most of it is in the electronic origins, it must be due to a static odd component in the ligand field. Figure 6c shows the polarized emission for $[Rh(bpy)_3](PF_6)_3:Cr^{3+}$ with and without an external magnetic field parallel to the c axis at 1.4 K. Depolarization is estimated to be $\sim 30\%$.

In Figure 7 the schematic splitting of the $^4A_2$ and the ^2E states in a trigonal ligand field and ed selection rules in the $D_3{}^*$ double group are shown.[1] The fact that, with $H \parallel c = 5$ T and at a temperature of 1.4 K, R_1 disappears completely in π and R_2 in σ (Figure 5b) leads to an unambiguous assignment of the two lines: R_1 corresponds to the $^4A_2 \rightarrow {}^2E(\bar{E})$ transition and R_2 to $^4A_2 \rightarrow {}^2E(2\bar{A})$; i.e., $D(^2E) = E(\bar{E}) - E(2\bar{A}) = -19.5$ cm^{-1}. From the

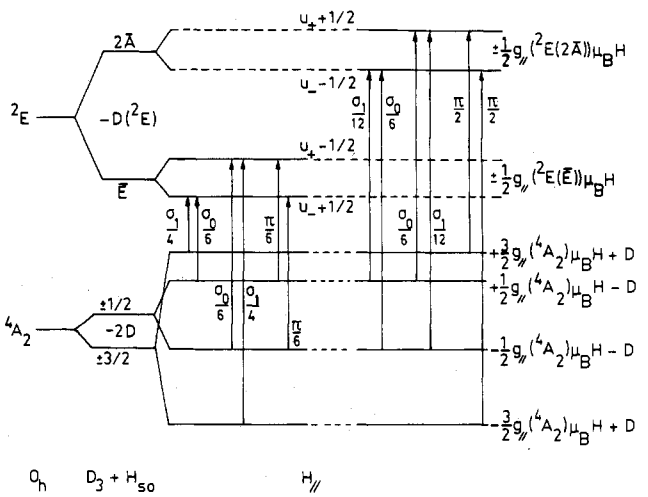

Figure 7. Schematic splittings of the $^4A_2$ ground state and the ^2E first excited state of d^3 under the effects of spin–orbit coupling, a trigonal ligand field, an external magnetic field $H \parallel c$, and ed selection rules.

temperature dependence of R_2 in π we can furthermore deduce the sign of the ground-state zero-field splitting $2D = E(\pm^3/_2) - E(\pm^1/_2)$: the $^4A_2(\pm^3/_2)$ component must be below the $^4A_2(\pm^1/_2)$ component. In fact, we can perform a Boltzmann population analysis of the temperature dependencies of the peaks that either originate totally from $^4A_2(\pm^3/_2)$ or $^4A_2(\pm^1/_2)$ in zero field, i.e. all except R_1 in σ. Figure 8 shows the experimental temperature dependence of R_2 in π and σ and R_1 in π for $[Cr(bpy)_3](PF_6)_3$ and R_2 in σ for $[Rh(bpy)_3](PF_6)_3:Cr^{3+}$. The Boltzmann population analysis (least-squares fit) using all three curves for $[Cr(bpy)_3](PF_6)_3$ with $2D$ and relative dipole strengths as free parameters and just the one curve with only $2D$ as the parameter for $[Rh(bpy)_3](PF_6)_3:Cr^{3+}$ resulted in $2D = -0.82$ (2) cm^{-1} for the former and -1.03 (4) cm^{-1} for the latter. These values compare very well with the results from EPR, especially with the $|2D| = 1.038$ cm^{-1} at 85 K for $[Rh(bpy)_3](PF_6)_3:Cr^{3+}$. The relative dipole strengths (relative to R_2 in π) are summarized in Table IV. From

(20) Ferguson, J. *Prog. Inorg. Chem.* **1975**, *14*, 171.

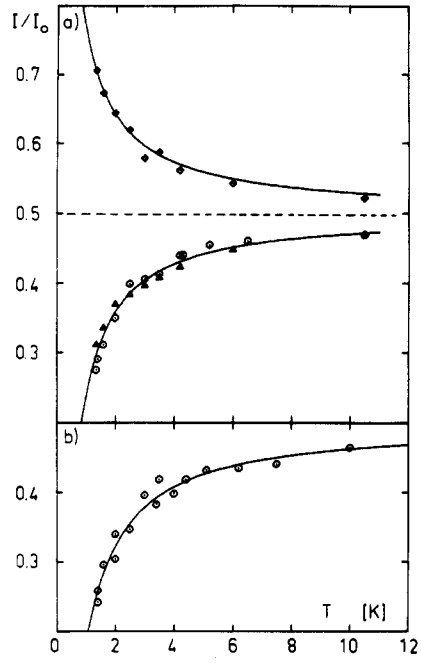

Figure 8. Boltzmann distribution analysis of the $^4A_2 \rightarrow {}^2E$ transition for (a) $[Cr(bpy)_3](PF_6)_3$ and (b) $[Rh(bpy)_3](PF_6)_3:Cr^{3+}$: (○) $^4A_2 \rightarrow {}^2E(2\bar{A})$; (△) $^4A_2 \rightarrow {}^2E(\bar{E})$ in π; (◇) $^4A_2 \rightarrow {}^2E(2\bar{A})$ in π; (—) analysis calculated with (a) $2D = -0.82$ cm^{-1} and (b) $2D = -1.03$ cm^{-1}.

Table IV. Relative Dipole Strengths of the Components of the $^4A_2 \rightarrow {}^2E$ Transition

	$^2E(\bar{E})$		$^2E(2\bar{A})$	
	σ	π	σ	π
$^4A_2(\pm^3/_2)$	~0.14			1
$^4A_2(\pm^1/_2)$	~1.10	0.38	1.22	

the σ spectrum with $H \parallel c$ it is also possible to estimate the relative dipole strengths for R_1 in σ, which was not used in the above analysis. If only spin–orbit coupling to the $^4T_2$ state in the octahedral limit is taken into account as the intensity mechanism for the spin-forbidden transitions, as was done by Sugano and Tanabe[1], then $\pi = \sigma_0 = \sigma_1$. This is clearly not so in our case. However, the group-theoretical relation of the π intensities ($1:^1/_3$ for $I(^4A_2 \rightarrow E):I(^4A_2 \rightarrow 2\bar{A})$) is still valid, and with $\sigma_0 \sim 3.3\pi$ and $\sigma_1 \sim 0.28\pi$, the experimental intensities listed in Table III can all be reproduced satisfactorily. Compared to the case of $2[Cr(en)_3]Cl_3 \cdot KCl \cdot 6H_2O$, where the observed intensities are close to the octahedral limit,[21] the σ intensity is enhanced with respect to π in $[Cr(bpy)_3](PF_6)_3$.

From the spectra with $H \parallel c$ and $H \perp c$, excited-state g values can be estimated by using shifts and splittings (see Table III). Due to the relatively large half-width of the bands (3–4 cm^{-1}) the accuracy of these g values is limited. The most accurate estimates can be obtained by using the formulas

$$g_\parallel(2\bar{A}) = 3g_\parallel(^4A_2) - 2\Delta_1/(\mu_B H_\parallel)$$
$$g_\parallel(\bar{E}) = 2\Delta_2/(\mu_B H_\parallel) - g_\parallel(^4A_2) \quad (3)$$

where Δ_1 is the observed shift of the $^4A_2 \rightarrow {}^2E(2\bar{A})$ absorption band in the external field and Δ_2 is the shift in the $^4A_2 \rightarrow {}^2E(\bar{E})$ emission band, both in the respective π spectra at 1.4 K (see Figure 6a,c) Table III also contains literature g values for $2[Cr(en)_3]Cl_3 \cdot KCl \cdot 6H_2O$.[9]

Full d^3 LF calculations (electrostatic interaction with Racah parameters B and C, spin–orbit coupling ζ, octahedral LF $10Dq$, trigonal component to the LF with K and K', and orbital reduction factor β (for details see the Appendix)) show that the four quantities $2D$, $D(^2E)$, $g_\parallel(^2E(\bar{E}))$ and $g_\parallel(^2E(2\bar{A}))$ are strong functions of K and K', somewhat weaker functions of ζ and β, and hardly dependent at all on B, C, and $10Dq$. $\zeta = 200$ cm^{-1} is known from the reduction in ground-state g values (see section 3.2), and $\beta = 0.71$ is given by the energy of ^2E relative to the ground state.[20] This leaves us with only the two parameters K and K' determining our four quantities. For Cr^{3+} in ruby, emerald, and spinels this procedure works very well, and in each case a unique pair of K and K' values can be found, so that for all four quantities calculated and experimental values agree simultaneously. In our case, this is neither possible for neat $[Cr(bpy)_3](PF_6)_3$ nor dilute $[Rh(bpy)_3](PF_6)_3:Cr^{3+}$. $D(^2E)$ is more sensitive to K than to K' whereas its g values and the ground-state zfs are more sensitive to K'. With $D(^2E) = -19.5$ cm^{-1} the second-order expression of Sugano and Tanabe[1] gives $K \sim -230$ cm^{-1}, and taking for instance $K = -230$ cm^{-1} and $K' = 240$ cm^{-1}, we calculate $D_{calcd}(^2E) = -19.5$ cm^{-1}, $g_\parallel(^2E(\bar{E})) = -1.69$, and $g_\parallel(^2E(2\bar{A})) = 2.17$, which are all in good agreement with the experimental values observed for $[Rh(bpy)_3](PF_6)_3:Cr^{3+}$. However, the calculated ground-state zfs is $2D_{calcd} = 0.18$ cm^{-1}, which is far from the experimental value $2D_{expt} = -1.03$ cm^{-1}. To explain this splitting within the d^3 basis, a $K' \approx -750$ cm^{-1} would be required.

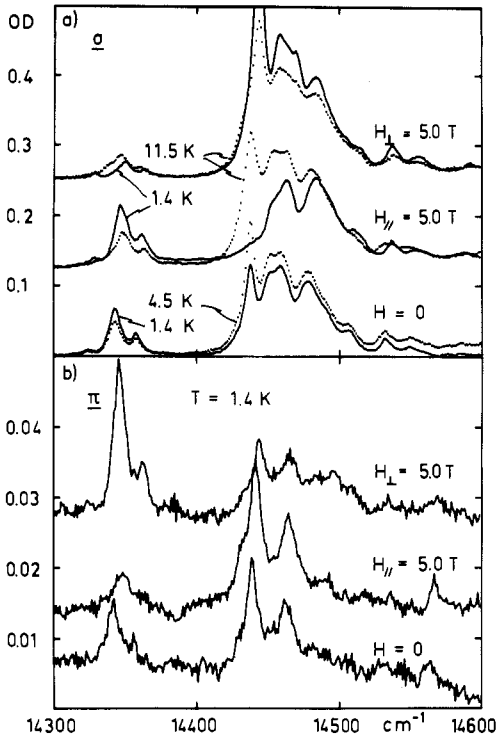

Figure 9. Polarized absorption (a) and Zeeman spectra (b) in the region of $^4A_2 \rightarrow {}^2T_1$ electronic origins at 1.4 K in $[Cr(bpy)_3](PF_6)_3$.

The facts (a) that the intensities within the $^4A_2 \rightarrow {}^2E$ multiplet, although not violating any group-theoretical considerations, are not in agreement with intensities calculated from spin–orbit coupling of ^2E to $^4T_2$ only and (b) that the ground-state zfs does not at all fit with the ^2E parameters indicate that low-energy charge-transfer states play an important role.

Any model that only takes into account geometrical distortions from octahedral symmetry results in a positive K for a contraction of the coordination octahedron along the trigonal axis such as in $[Cr(bpy)_3](PF_6)_3$ (see Table I). However, Orgel[23] predicted that, in tris chelate complexes where the frontier π orbitals of one bidentate ligand are phase-coupled via its π-electron system, the t_2 orbitals on the metal would be split quite considerably even if the trigonal distortion of the complex was small. Ceulemans et al.[24] showed that for a ligand with a low-lying χ-type HOMO (symmetric under C_2), the a_1 orbital of the t_2 set would be de-

(21) Dubicki, L., unpublished results.
(22) Hauser, A.; Murugesan, R., unpublished results.
(23) Orgel, L. E. *J. Chem. Soc.* **1961**, 3683.
(24) Ceulemans, A.; Dendooven, M.; Vanquickenborne, L. G. *Inorg. Chem.* **1985**, *24*, 1153.

stabilized with respect to the e orbitals, resulting in a negative contribution to K. The HOMO of bpy is indeed χ type,[23,25] and we observe a negative K.

3.3.2. The $^4A_2 \rightarrow {}^2T_1$ Transition. Figure 9 shows the polarized single-crystal absorption spectra of $[Cr(bpy)_3](PF_6)_3$ in the region of the $^4A_2 \rightarrow {}^2T_1$ electronic origins. We make this assignment due to the fact that there are no vibronic sidebands of ^2E of comparable intensity at corresponding energies in the emission spectrum. The most striking point to note is the strong σ polarization of the band system and its intensity in this polarization, which is comparable to the $^4A_2 \rightarrow {}^2E$ intensity. This is completely different from what is observed in the same $^4A_2 \rightarrow {}^2T_1$ transition in for example $2[Cr(en)_3]Cl_3 \cdot KCl \cdot 6H_2O$,[10] where no such strong polarization is observed and the total intensity is smaller than the $^4A_2 \rightarrow {}^2E$ intensity.

In D_3* the $^2T_1$ state is split into three Kramer's doublets: $2\bar{A}$, $\bar{E}^a$, and $\bar{E}^b$. The prominent line at 14438 cm^{-1} can easily be identified as the $^4A_2 \rightarrow {}^2T_1(2\bar{A})$ transition from its temperature and field dependence; i.e., $^4A_2(\pm^3/_2) \rightarrow {}^2T_1(2\bar{A})$ is forbidden in σ. From the shift in π can be estimated $g_\parallel(^2T_1(2\bar{A})) = 3.5$, which supports the assignment, because it is the only state in the multiplet for which $g_\parallel$ can be large. Unfortunately, the remainder of the spectrum is rather complicated. From the polarization behavior we can tentatively assign one of the $^4A_2 \rightarrow {}^2T_1(\bar{E})$ transitions to the band at ~14350 cm^{-1} and say that the other one is somewhere in the set of peaks toward higher energy from $^4A_2 \rightarrow {}^2T_1(2\bar{A})$. However, the number of observed bands in this region is puzzling. It looks as if every band is doubled with an energy separation of ~14 cm^{-1}. A low-energy phonon seems unlikely in view of the fact that none are observed for the $^4A_2 \rightarrow {}^2E$ transition. An alternative explanation lies in the crystal structure: there are two species with slightly different geometries present. They see of course slightly different ligand fields, and if the difference is large enough, one would of course observe a doubling of each line. The zfs of ^2E is largely dependent on K, which according to Orgel is given not so much by the geometry of the complex but rather by the fact that the π orbitals within one bidentate ligand are phase-coupled.[23] The $^2T_1$ zfs is much more susceptible to K', which is more dependent on geometrical distortions (σ bonding). Small differences in K' between the two species would effectively account for the apparent doubling of lines in the $^4A_2 \rightarrow {}^2T_1$ transition without affecting the ^2E state.

3.3.3. $^4A_2 \rightarrow {}^4T_2/{}^2T_2$ Transitions. In Figure 4 the polarized single-crystal absorption spectra of the region of $^4A_2 \rightarrow {}^4T_2/{}^2T_2$ electronic origins on the tail of a low-energy charge-transfer band are shown. The spectra show a lot of fine structure between 20000 and 21000 cm^{-1}. At higher energy a steady rise toward the CT region is observed. König and Herzog[19] attributed a shoulder at 23400 cm^{-1} in the solution spectrum to the $^4A_2 \rightarrow {}^4T_2$ band maximum. We were not able to see this shoulder, as ODs at energies greater than ~22000 cm^{-1} were too high even in the dilute crystal.

The first sharp band at 19999 cm^{-1} is of $2\bar{A}$ character, and with the vibrational frequencies of 164, 372, and 665 cm^{-1} observed in the emission spectrum, most of the prominent lines can be assigned as vibronic sidebands to the line at 19999 cm^{-1}. The close agreement of the vibrational energies associated with the $2\bar{A}$ band with the ground-state vibrational energies makes it more likely to belong to a d–d rather than a CT transition. On the other hand, its vibronic structure is much more pronounced than that for the $^4A_2 \rightarrow {}^2E$ and $^2T_1$ transitions, and this points to its being a component of the transition to the $^4T_2$ state with a $t_2{}^2e$ configuration rather than to the $^2T_2$ state with a $t_2{}^3$ configuration. There is no evidence at this stage for any of the bands in this region belonging to the $^4A_2 \rightarrow {}^2T_2$ transition.

4. Conclusions

We have presented results from EPR and optical spectroscopy and been able to unambiguously assign several of the observed bands in the absorption spectrum and estimate ground-state and some excited-state g values and zero-field splittings. It is not possible to explain the finer details of the electronic structure by using a full d^3 LF calculation including the trigonal field. This is in contrast to ruby, emerald, and spinels.[3-5] However, it should be noted[26] that already for $2[Cr(en)_3]Cl_3 \cdot KCl \cdot 6H_2O$ LF theory runs into difficulties, although the discrepancy between $2D_{calcd}$ values obtained with K and K' from ^2E is not quite as dramatic as that for $[Cr(bpy)_3](PF_6)_3$. Intensities are enhanced in σ for both the ^2E and the $^2T_1$ transitions as compared to those for $[Cr(en)_3]^{3+}$ compounds. Both of these facts indicate that in $[Cr(bpy)_3](PF_6)_3$ the extremely low-lying (ligand-to-metal) charge-transfer states[27] are important, as they are only slightly higher in energy than the $^4T_2$ state. Low-symmetry fields could mix them quite efficiently into the quartet LF states, i.e. even into the ground state, thus being responsible for the large ground-state zero-field splitting.

The mixing of charge-transfer states would also help to qualitatively explain the enhanced σ intensity. In $[Cr(bpy)_3](PF_6)_3$ the lowest energy CT transition is most probably ligand-to-metal, namely from the HOMO of the π system on bpy to a t_2 orbital on the metal.[28] Such a transition would be mainly σ polarized, and if the d–d transitions get some of their intensity from it, they would of course show enhanced intensity in σ polarization. In $[Cr(en)_3]^{3+}$ compounds there is no such low-energy CT transition with similar polarization properties.

The most disquieting thing is the fact that even for $[Cr(en)_3]^{3+}$ compounds the full d^3 LF calculation gives rather poor results. It would be of interest to study $[Cr(NH_3)_6](ClO_4)_2Cl \cdot KCl$, where the site symmetry of the $[Cr(NH_3)_6]^{3+}$ complex is D_{3d}[8] and the electronic origins of the d–d transitions have only md intensity, and where the lowest energy charge-transfer transition is well removed from the $^4A_2 \rightarrow {}^4T_2/{}^2T_2$ transitions, in order to establish at exactly what point LF theory for trigonal fields is no longer capable of explaining the observed splittings and g values of the $^4A_2$ and the ^2E states with one set of trigonal LF parameters.

Acknowledgment. We thank Dr. Lucjan Dubicki for helpful discussions.

Appendix

The Hamiltonian for the full d^3 LF calculation takes the form

$$\hat{H} = \hat{H}^0 + \hat{H}'$$

$$\hat{H}' = \sum_{i<j}(1/r_{ij}) + \hat{V}_{LF} + \hat{H}_{so} + \hat{H}_m$$

$$\hat{V}_{LF} = \hat{V}_{oct} + \hat{V}_{trig}$$

$$\hat{H}_{so} = \zeta \sum_i \vec{s}_i \vec{l}_i$$

$$\hat{H}_m = \mu_B \vec{H}(\vec{L} + 2\vec{S})$$

where $\sum(1/r_{ij})$ is the electrostatic interaction, $\hat{V}_{LF}$ is the ligand field with its octahedral and its trigonal part, $\hat{H}_{so}$ is the spin–orbit coupling, and $\hat{H}_m$ is an external magnetic field. $\hat{H}^0$ is the free-ion Hamiltonian without the electron–electron interaction, resulting in the d^3 configuration with its 120-fold degeneracy, which is the starting point of the perturbation calculation. The matrix elements of $\hat{V}_{LF}$ ($10Dq = \langle e|\hat{V}_{oct}|e\rangle - \langle t_2|\hat{V}_{oct}|t_2\rangle$, $K = \langle t_2x_\pm|\hat{V}_{trig}|t_2x_\pm\rangle$, $K' = -(1/2^{1/2})\langle t_2x_\pm|\hat{V}_{trig}|eu_\pm\rangle$), $\hat{H}_{so}$, and $\hat{H}_m$ were calculated within the symmetry-adapted strong-field basis of Tanabe et al.,[29] with t_2x_0 transforming as A_1 and $t_2x_\pm$ and $eu_\pm$ as E of D_3. The matrix elements for the electrostatic interaction were taken from Tanabe et al.[29] with the Racah parameters B and C. The individual parts of the total matrix were checked separately by comparing the results of trial calculations to results of literature matrices; i.e.,

(25) Gondo, Y. *J. Chem. Phys.* **1964**, *41*, 3928.

(26) $K \approx -210$ cm^{-1} and $K' \approx 300$ cm^{-1} give ^2E splitting and g values in good agreement with the experimental values, but $2D_{calcd} = 0.39$ cm^{-1}.

(27) Fergusson, J. E. *Aust. J. Chem.* **1971**, *24*, 247.

(28) Ceulemans, A.; Vanquickenborne, L. G. *J. Am. Chem. Soc.* **1981**, *103*, 2238.

(29) Tanabe, Y.; Sugano, S.; Kamimura, H. *Multiplets of Transition Metal Ions in Crystals*; Academic: New York, 1970.

the LF matrix was checked against the weak-field matrix of McFarlane[3] by setting $\zeta = 0$, the spin–orbit coupling matrix was checked against the Eisenstein matrix[30] by setting K and $K' = 0$, and the resulting g values from the external magnetic field matrix were checked with the Lande formula for g values of the free ion[18] by setting $10Dq = K = K' = 0$. In the calculations appropriate for $[Cr(bpy)_3]^{3+}$ the Racah parameters B and C were reduced from their free-ion values of 1030 and 3850 cm^{-1},[18] respectively, by an orbital reduction factor $\beta = E(^2E_{complex})/E(^2E_{free\ ion}) = 0.71$.[20]

(30) Eisenstein, J. C. *J. Chem. Phys.* **1961**, *34*, 1628.

Notes

Contribution from the Department of Chemistry, D-006, University of California, San Diego, La Jolla, California 92093

Perhalogenated Tetraphenylhemins: Stable Catalysts of High Turnover Catalytic Hydroxylations

Teddy G. Traylor* and Shinji Tsuchiya

Received October 2, 1986

Recent interest in biochemical, biomimetic, and synthetic hydroxylation reactions[1-3] that are catalyzed by metalloporphyrins has prompted us to seek more robust catalysts. We recently reported tetraphenylhemin derivatives bearing, as 2,6-substituents on the phenyl rings, groups that are both electronegative and bulky.[4,5] Of these, iron(III) tetrakis(2,6-dichlorophenyl)porphyrin chloride ($\mathbf{1}^+Cl^-$) has become a widely used catalyst for epoxidation reactions.[5-8] However, neither this compound nor the iron(III) tetrakis(2,6-ditrifluoromethylphenyl)porphyrin[9] are sufficiently robust to afford high turnover catalyzed hydroxylation without catalyst loss.[4] We have therefore turned to further halogenation of this compound to provide iron porphyrins that are resistant to attack by the strong oxidizing agents generated as intermediates. This strategy has been successful. We describe here a simple bromination that converts **1**-Zn to its octabromo derivative, affording a very robust iron porphyrin catalyst, Fe^{III}88TPP, in good yield.

Experimental Section

The zinc tetrakis(2,6-dichlorophenyl)porphyrin complex (**1**-Zn) (1 g, 0.001 M)[4,10] was dissolved in carbon tetrachloride (100 mL), and *N*-bromosuccinimide (1.85 g, 0.01 M) was added to this solution.[11] This solution was refluxed under air for 5 h and allowed to stand at room temperature for 2 h. The reaction mixture was reduced to dryness and the resulting black solid chromatographed on alumina, eluting with chloroform. The first moving fraction was collected. Evaporation of solvent yielded 1.1 g of the brominated zinc complex (**2**-Zn) (yield 71%). The 300-MHz NMR spectrum of this compound consisted of a complex phenyl region at 7.2–7.8 ppm but no peaks due to pyrrole protons.[12] The UV–visible spectrum is listed in Table I along with other spectra.

The zinc complex (1 g) was dissolved in 100 mL of dichloromethane and 10 mL of trifluoroacetic acid was added. This mixture was stirred for 5 h and poured into ice. The organic layer, which slowly separated, was removed and washed with water and with saturated aqueous sodium bicarbonate. The evaporation of the solvent gave the desired porphyrin (0.75 g). This porphyrin was purified by alumina column chromatography using chloroform as solvent. Again the NMR was characterized by a complex phenyl proton pattern at 7.2–7.8 ppm. The parent peak in the mass spectrum consisted of at least 16 lines centered at 1521, in agreement with the calculated M_r. The UV-visible spectrum listed in Table I shows a Soret absorption at 462 nm. This is 48-nm red shifted from the starting octachloroporphyrin, in good agreement with the approximately 6 nm/Br shift found by Callot for the mono- to tetrabrominated tetraphenylporphyrins. The porphyrin was converted to the Fe(III) derivative, $\mathbf{2}^+Cl^-$, by the standard $FeBr_2$/DMF procedure,[13] followed by purification from unreacted porphyrin by alumina chromatography. The UV–visible spectrum is listed in Table I. The NMR of $\mathbf{2}^+Cl^-$ consisted of absorbances at 14.42, 14.01 (meta protons), and 7.48 (para) ppm. This compares with 13.98, 12.67 (meta), 8.1 (para), and 80.5 (pyrrole protons) ppm for $\mathbf{1}^+Cl^-$, indicating the absence of pyrrole protons in $\mathbf{2}^+Cl^-$.

Table I. UV–Visible Spectra of Derivatives of 88TPP (**2**)

	λ_{max}, nm (ϵ^a)				
porphyrin		462 (100)	557 (7)	598 (2.7)	603 (sh)
Zn complex		468 (100)	602 (6)	600 (sh)	
Fe^+Cl^- complex	400 (84)	453 (100)	580 (sh)		
Fe^+OH^- complex		424 (100)	495 (87)	600 (14)	

[a] All extinction coefficients are relative to the Soret maximum in the species and are not absolute nor related to other derivatives.

Results and Discussion

The remarkable stability of the octabromooctachlorohemin toward destruction during catalyzed hydroxylation is demonstrated by the following experiments. Portions of a solution containing 1 M norbornane and 0.06 M pentafluoroiodosylbenzene[4] (as a suspension) were treated separately with tetraphenylhemin chloride, $\mathbf{1}^+Cl^-$, and $\mathbf{2}^+Cl^-$. In the first case the solution instantly bleached and little or no oxidant dissolved. With $\mathbf{1}^+Cl^-$ about 75% hemin destruction was accompanied by dissolution of the oxidant and about 40% yield of 2-norborneols. With $\mathbf{2}^+Cl^-$, a 75% yield of norborneols was obtained and no hemin loss was observed. Diluted spectra of the starting and final solutions had the same Soret absorbance at 453 nm. In another comparison a solution of 0.3 M cholestane (Aldrich) and 10^{-4} M hemin (either $\mathbf{2}^+Cl^-$ or tetrakis(pentafluorophenyl)hemin chloride (Aldrich)) was shaken with 0.06 molar equiv of PFIB until the solid dissolved or bleaching occurred. With $\mathbf{2}^+Cl^-$, 40% loss of the Soret band occurred whereas the tetrakis(pentafluorophenyl)hemin chloride was completely bleached. At higher hemin and substrate concentrations there was no loss of $\mathbf{2}^+Cl^-$ and about 50% loss of the fluorinated hemin.

Epoxidation of 4,4-dimethyl-1-pentene using $\mathbf{2}^+Cl^-$ under the conditions that resulted in complete conversion to *N*-alkylhemin with $\mathbf{1}^+Cl^-$[8] gave no change in the spectrum of $\mathbf{2}^+Cl^-$. Therefore it is much less prone to "suicide labeling" than are other hemins.

In the soluble system (CH_2Cl_2, CF_3CH_2OH, H_2O)[14] where tetraphenylhemin, tetramesitylhemin, and $\mathbf{1}^+Cl^-$ are destroyed at

(1) White, R. E.; Coon, M. J. *Annu. Rev. Biochem.* **1980**, *49*, 315.
(2) Sheldon, R. A.; Kochi, J. K. *Metal-Catalyzed Oxidations of Organic Compounds*; Academic: New York, 1981.
(3) Guengerich, F. P.; McDonald, T. L. *Acc. Chem. Res.* **1984**, *17*, 9.
(4) Traylor, P. S.; Dolphin, D.; Traylor, T. G. *J. Chem. Soc., Chem. Commun.* **1984**, 279.
(5) Renaud, J.; Battioni, P.; Bartoli, J. F.; Mansuy, D. *J. Chem. Soc., Chem. Commun.* **1985**, 888.
(6) de Poorter, B.; Meunier, B. *Tetrahedron Lett.* **1984**, *25*, 1895.
(7) Dicken, C. M.; Woon, T. C.; Bruice, T. C. *J. Am. Chem. Soc.* **1986**, *108*, 1636.
(8) Mashiko, T.; Dolphin, D.; Nakano, T.; Traylor, T. G. *J. Am. Chem. Soc.* **1985**, *107*, 3735.
(9) Tsuchiya, S., unpublished work.
(10) Bromination of the free porphyrin was less successful.
(11) This is a variation of the method of: Callot, H. J. *Bull. Soc. Chim. Fr.* **1974**, 1492.
(12) A later fraction had a small amount of pyrrole proton NMR and a Soret absorbance at 450 nm indicating some hexa or heptabromide.
(13) Adler, A. D.; Longo, F. R.; Kampos, F.; Kim, J. *J. Inorg. Nucl. Chem.* **1970**, *32*, 2443.
(14) Traylor, T. G.; Nakano, T.; Dunlap, B. E.; Traylor, P. S.; Dolphin, D. *J. Am. Chem. Soc.* **1986**, *108*, 2782.

0020-1669/87/1326-1338$01.50/0